

Mixing and Dissolution Processes of Pharmaceutical Bulk Materials in Stirred Tanks: Experimental and Numerical Investigations

Thomas Hörmann,[†] Daniele Suzzi,[†] and Johannes G. Khinast^{*,†,‡}

[†]Research Center Pharmaceutical Engineering GmbH, Inffeldg. 21A, Graz, Austria

[‡]Institute for Process and Particle Engineering, Graz University of Technology, Inffeldg. 21A, Graz, Austria

ABSTRACT: Numerical analysis of mixing and dissolution processes is becoming increasingly important for gaining a process understanding and thus optimizing the production. Due to the increasing costs and shortage of raw materials, “in-silico” techniques are currently employed together with standard experimental analyses. Numerical simulations have proven to be a useful tool for understanding and optimizing industrial mixing problems. However, such simulations are still in the research phase. Although Computational Fluid Dynamics (CFD) is a well-developed and validated method, for more complex applications (e.g., industrial mixing) much work is still required to obtain reliable results quickly enough. In this work we focused on the simulation of mixing and dissolution of a bulk powder in a moderately viscous solution in an unbaffled stirred tank reactor typically used in the chemical and pharmaceutical industries. Estimations were made with regard to optimizing batch sizes, tank geometry, impeller type, and placement and process variables, such as the impeller agitation speed. In addition, the vortex formation of the liquid surface, the feeding position of the bulk powder, and the dissolution process of the solid particles that represent the bulk powder were manipulated. Finally, a quantitative comparison of different stirring systems and scale-up studies was prepared. The time-dependent and turbulent flow of the mixture was studied by solving the Reynolds-averaged Navier–Stokes equations. The numerical predictions of the flow field were validated by means of high-speed camera images and particle image velocimetry postprocessing techniques.

INTRODUCTION

Stirring, mixing, blending, homogenization, and emulsification are essential unit operations in the manufacture of many pharmaceutical products and are in most cases carried out in agitated tanks made of steel and sometimes equipped with a glass liner. Another important operation is the dissolution of solids in a liquid phase.¹

A large number of studies have therefore focused on analyzing the (multiphase) flow in agitated vessels, including numerical and experimental studies. Different flow regimes have been identified, depending on the range of the Reynolds (Re) number, and also different systems including various impeller types and baffle systems or systems with no baffles at all. It is well-known that the impeller Re number is an important indicator of the flow inside the tank. At Re numbers lower than 100 the flow is typically laminar. Turbulent conditions, where the power number is usually independent of Re, are obtained for Re numbers exceeding 10,000 for baffled systems. Between these regions a transitional regime is obtained depending on the impeller type and system parameters.² In the transitional, but also in the turbulent flow regime baffles may be used to minimize vortex formation and to improve the top to down mixing behavior within an agitated tank.

In the computational description of stirred tanks via CFD turbulence effects can be reproduced using various turbulence models, for example, the k - ϵ model, the RNG- k - ϵ model,⁴ the k - ω model, the Shear Stress Transport (SST) model,⁵ or the Reynolds stress model (RSM).⁶ In addition to turbulence modeling, the main difficulty is the description of the rotor. In order to account for the impeller rotation, different rotor-stator

models are used, i.e., the multiple reference frames (MRF) and the sliding-mesh (SM) methods or a combination of both. The MRF method is a steady-state approach, while SM provides a transient description of the flow. Those different models and methods were considered by many researchers. For example, Bakker et al.⁷ described SM simulations of laminar flow, Lamberto et al.⁸ analyzed the laminar mixing utilizing a MRF approach, and Wang et al.⁹ compared SM-CFD simulations and PIV measurements, for different flow regimes. Comparisons between measurements and results of agitated tank CFD simulations can be found also in the work of Aubin et al.^{10,11} (Laser Doppler velocimetry (LDV) measurements) and Montante et al.¹² (LDA measurements). In the work of Kumaresan et al.¹³ several impeller designs were investigated by means of SM-CFD simulations (k - ϵ turbulence model). The results were compared to the measurements of the power number, the mixing time, and the flow patterns. The impact of surface modeling, i.e., the prescription of a flat or simulation of a (realistic) curved free liquid surface was analyzed by Ciofalo et al.¹⁴ In their work an iterative procedure (based on MRF) was implemented to determine the free surface profile. All contributions mentioned above are based on the Reynolds-Averaged Navier–Stokes (RANS) approach.

Contrary to the RANS approach, Large-Eddy Simulation (LES) methods solve the time-dependent Navier–Stokes equations for

Received: February 3, 2011

Accepted: September 23, 2011

Revised: August 26, 2011

Published: September 23, 2011

the mean flow and the largest eddies.¹⁵ Only the smaller eddies below a certain threshold (often the grid size is used) are described via subgrid models.⁴ Many recent reviews address the agreement between the predicted and the measured turbulence levels obtained by using LES methods.^{16–19} It was shown, that LES can generate more accurate results than RANS simulations. Nevertheless, in practice the use of LES as a design tool is still limited due to the costs associated with its computational power requirements and the calculation time.²⁰ Direct numerical simulations (DNS), which solve the Navier–Stokes equations without averaging or modeling of the turbulence are time-consuming and require expensive computational hardware. Thus, they are not feasible for most industrial applications and are not discussed here further.

In addition to the analysis of fluid flow, numerous publications have focused on solid–liquid mixing in stirred tanks. For example, Hosseini et al.²¹ presented a CFD model for studying the effects of operating conditions and design parameters on the mixing quality for solid–liquid mixing operations. Armenante and Nagamine²² discussed the effect of the off-bottom impeller clearance on the minimum agitation speed for complete suspension in stirred tanks. Derksen¹⁶ coupled a LES and a Lagrangian description of spherical, solid particles in order to investigate the particle dynamics in a stirred tank. Hartmann et al.¹⁷ studied dissolution processes of solid particles suspended in a turbulent flow of a Rushton turbine stirred tank numerically by LES. Myers and Bakker²³ provided impeller selection guidelines for solid suspension with up-pumping pitched-blade and high-efficiency impellers. Shekhar et al.²⁴ successfully simulated the flow and mixing characteristics in an unbaffled vessel for a wide range of Reynolds numbers employing the SM technique for the impeller motion description.

Also experimental investigations have been carried out on solid–liquid mixing, which have been described in detail in Paul et al.² The Computer Automated Radioactive Particle Tracking (CARPT) technique was employed by Guha et al.²⁵ to investigate the solid hydrodynamics in dense solid–liquid suspensions (2.5–19% solids loading w/w) in a stirred tank. The results provide useful information to efficiently assess the ability of CFD models in calculating the particle dynamics in stirred reactors. Özcan-Taskin et al.²⁶ investigated the effect of the impeller-to-tank ratio on the drawdown of solids. Solid dissolution processes within stirred tank reactors were studied by Pangarkar et al.²⁷ The main focus of their work was to find and discuss correlations between the particle-liquid mass transfer coefficient and the system configurations, operating parameters, and physical properties. Khazam et al.²⁸ presented experimental investigations regarding floating solids in stirred vessels. Different configurations of the impellers and baffle arrangements were investigated to find an optimum between the impeller speed and its placement in order to improve the solid distribution and avoiding air entrainment.

Investigations using the USP Dissolution Testing Apparatus II (USP Apparatus II)²⁹ were also utilized to improve the understanding of dissolution processes in stirred tanks. Many authors recently verified the hydrodynamics of the USP Apparatus II, as, for example, Bai et al.³⁰ that employed both experimental and “in silico” techniques, including laser-Doppler velocimetry (LDV),^{31,32} particle image velocimetry (PIV),³³ laser-induced fluorescence (LIF),³⁴ and computational simulations.^{30,34–37}

The objective of this paper is to analyze, evaluate, and optimize solid–liquid mixing and dissolution operations. For that purpose,

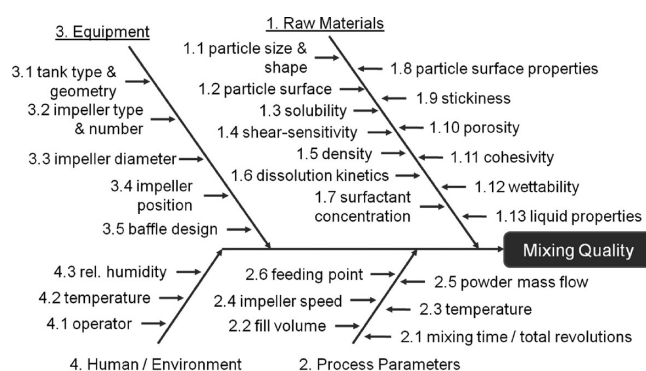


Figure 1. Ishikawa diagram of mixing and dissolution of solids in liquid.³⁹

a RANS-based CFD method was developed combined with the 3-equation k - ϵ - f turbulence model.³⁸ Furthermore, an iterative procedure addresses the vortex formation at the air–liquid interface. The computationally predicted fluid flow was validated by PIV measurements. Suspension and dissolution of solid particles was taken into account as well. Polyethylene glycol (PEG 6000) particles were used as a model substance for the dissolution simulations. PEG 6000 was used because it is water-soluble, appears in powder form, and is widely used in the pharmaceutical and chemical industries. Furthermore, it strongly changes the viscosity of water upon dissolution.

In summary, the goals of this study are

- the experimental characterization of the flow via PIV
- the development and validation of a CFD tool for simulating dissolution of solids in stirred tanks
- and the optimization of the mixing and dissolution process

Thus, the objective is to reliably predict the effect of the process parameters and material properties on the quality of the final product. In the language of Quality-by-Design, this study will associate the critical process parameters, such as tank design, rotation rate, and the critical material parameters, such as particle size, solubility, and wettability, with the critical product attributes. The validated tool represents the basis for the definition of the engineering design space for mixing processes in the pharmaceutical industry.

BACKGROUND

Dissolution and mixing in a stirred tank are influenced by many parameters, an overview of which is provided in an Ishikawa diagram in Figure 1.³⁹ Many of these parameters cannot be changed in a pharmaceutical manufacturing setting. For example, most of the physicochemical properties of a raw material are fixed, although variations do occur due to the batch-to-batch variability of APIs and excipients received from supplies companies. Similarly, in most cases the type of equipment that is used is fixed, requiring manufactures to adapt the process parameters (i.e., the changeable parameters) to the available tanks and systems.

While experiments typically do not allow change of most parameters, simulations are ideally suited to study the impact of all influences. For example, all equipment properties and the process parameters are adjustable in a simulation. This was done in the current study. Material properties have also a strong impact to the dissolution and mixing process. However, the porosity of the solid particles, the particle shape, the stickiness, the cohesivity, and the wettability will not be considered in this work, since

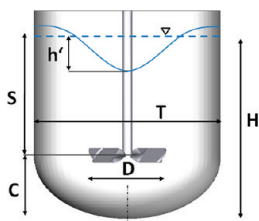


Figure 2. Characteristic dimensions of a stirred tank.

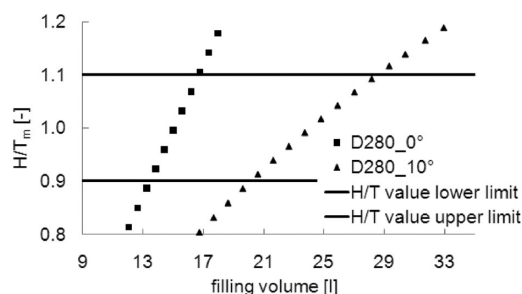


Figure 3. The H/T value as a function of filling volume for cylinder shaped (squares) and cone shaped (triangles) tanks. The horizontal lines denote the range in which operation is recommended. The diameter of the torispherical head is 0.28 m for both the cylinder-shaped and the conical-shaped tanks. The cone angle of the conical tank is 10° .

here, the powder particles are assumed to be already wetted spheres in a dense solid–liquid suspension.

Mixer System. In Figure 2 characteristic dimensions of a stirred tank system are provided. The main parts influencing the hydrodynamics are the tank type, the impeller, and the shaft as well as the baffles. The dimensions T , D , H , S , C , and b represent the vessel diameter, the impeller diameter, the filling level of the liquid, the submergence of the impeller, the bottom clearance, and the impeller blade height, respectively. Additional parameters are the baffle number, width, height, and position. The outlet is typically realized at the lowest point of the dished bottom.

Many tanks are cylindrical. However, there are also conical tanks, which are used as fermenters or as special crystallization units. The shape and size of the tank is defined by the process needs. For example, in industrial mixing the batch size might change from one production run to the next. Therefore, the tank size in a manufacturing setting should be chosen such that a wide range of batch sizes can be used while still assuring acceptable fill levels. A value of H/T near unity is considered a good choice for many single impeller mixing applications,¹ and typically the H/T ratio should be lower than 1.5 for one-impeller systems.²

In Figure 3 the H/T value is plotted as a function of the liquid volume of the tank for a cylindrically (squares) and conically (triangles) shaped tank with a cone angle of 10° . Both tanks have the same diameter of the torispherical head. For the definition of the H/T value of a cone-shaped tank the mean diameter of the tank was used, i.e., $T_m = (T_{\min} + T_{\max})/2$, where T_{\min} and T_{\max} represent the smallest and the largest diameters of the cone part of the vessel. The horizontal lines in Figure 3 denote the limits of the H/T ratio that were used in this work, i.e., 0.9 and 1.1 (H/T ratio = $1 \pm 10\%$). It can be seen that a cone-shaped tank provides a wider operating range, i.e., greater flexibility, which may be important in industrial settings as typically a series of

different capacity tanks are required. Thus, tank geometries that accommodate a wider range of filling-levels reduce equipment and maintenance costs, since fewer tanks are required. For this reason, cone-shaped tanks are often used. Nevertheless, their use is limited, especially with regard to solid–liquid applications as too-large cone angles prevent good top-to-bottom mixing.

The flow in the tank and the power consumption are generally characterized by the Re and the Newton (power) number Ne , which are defined as

$$Re = \frac{ND^2}{\nu} \quad (1)$$

and

$$Ne = \frac{P}{\rho N^3 D^5} = f(Re) \quad (2)$$

P , ρ , N , D , and ν represent the power input by the stirrer, the density of the liquid, the stirring speed, the impeller diameter as the characteristic length, and the kinematic viscosity of the liquid, respectively. As described above, the flow is laminar at a Re number of 10 and fully turbulent above $Re = 10^4$, with a transitional regime in between. A characteristic curve, i.e., $Ne = f(Re)$ is valid only for one impeller combination. However, at high Re numbers the power number reaches an asymptote (generally between 0.2 and 10),¹ which is typical for the impeller geometry used. Based on these characteristics, the stirrer type and the mixing conditions (e.g., for suspending powders) are chosen.⁴⁰ For stirred tanks with standard configuration, i.e., equipped with a pitched blade turbine PBT ($T/D = 3$; $C/D = 0.5$), propeller ($T/D = 3.33$; $C/D = 1.5$), or Ekato MIG ($T/D = 1.43$; $C/D = 0.15$), power characteristics are freely available in the literature.¹ However, for special configurations experimental studies are required to determine the power characteristics. Alternatively, high-fidelity CFD simulations can compute these characteristic curves and thus reduce the experimental effort.

Baffles and Powder Feeding. Mixing tanks often include baffles in order to increase the mixing rate, especially in the transitional and turbulent flow regime. Nevertheless, in the (bio-) pharmaceutical industry there are case-wise restrictions with respect to the use of baffles.⁴¹ Unbaffled vessels are preferentially adopted for laminar mixing, as some dead regions may exist in front of the baffles. Another reason may be the need to feed powders (e.g., lyophilized proteins) into the liquid vortex, thus enabling faster dissolution. Extensive liquid vortices are formed only in unbaffled systems.¹ Moreover, unbaffled tanks facilitate the clean-in-place/sterilize-in-place procedures that can be negatively affected by baffles, especially for suspensions or dissolving solids due to the gaps between the baffles and the tank wall.

In the case of dissolution processes the goal is to first suspend the solid in the liquid phase. This is achieved by contacting the solid with the liquid phase, which can be done in multiple ways, e.g., via surface feeding, high shear rotor-stator mixers, static-tube mixers, and bottom entry systems.² Nevertheless, in the pharmaceutical industry when the powder consists of sinking solids the powder is typically fed at the liquid surface via vortex feeding. The low shear stress (e.g., for proteins) and the losses in complex feeding machines are often quoted as the reason. Other common concerns include air entrainment and powder sticking to the walls and the impeller shaft, if solids are sticky upon wetting.² A common method to avoid this is vortex formation that is used to dose solids and disperse them in the liquid phase. The goal of

vortex feeding is to obtain a vortex away of the impeller shaft (and the walls), by locating the shaft eccentrically in the tank. When feeding the solids right into the liquid vortex, they will be entrained into the liquid without sticking at the wall and/or the impeller shaft.

Vortex formation is a function of the impeller diameter D , the level H' of the liquid above the impeller (see Figure 2), the Froude number Fr , and the Galilei number Ga . The Froude number Fr is defined by

$$Fr = \frac{N^2 D}{g} \quad (3)$$

whereas the Ga number is

$$Ga = \frac{Re^2}{Fr} = \frac{D^3 \rho^2 g}{\eta_{fl}^2} \quad (4)$$

Zlokarnik,¹ for example, reported an empirical equation for the vortex depth h' induced by a propeller

$$\frac{h'}{D} = 13.8 \cdot Fr \cdot (0.25 - Ga^{0.1}) \cdot \left(\frac{S}{D}\right)^{-0.33} \quad (5)$$

Contact angle and wettability and particle surface and porosity as well as density and stickiness of the particles are the main parameters controlling the powder feeding step and the entry of particles in the liquid. Once the particles are suspended, the dissolution kinetics determines the overall dissolution rate. The dissolution kinetics depend on the local mass transfer coefficient (which in turn is a function of suspension state and the local turbulence level), on the thermodynamics of the crystal, and on the equilibrium solubility at the fluid temperature. In the case of shear-sensitive materials, special care must be taken in order to avoid damage of the product due to high-shear mixing. In the case of highly viscous systems, homogenization is another distinct step.

Minimum Stirrer Speed for Suspension. Complete particle suspension is required for an efficient dissolution process. The Zwietering correlation defines the minimum necessary impeller speed N_{js} in order to just suspend the particles^{18,42} in baffled tanks

$$N_{js} = S \frac{d_{p0}^{0.2} \nu^{0.1} (g \Delta \rho)^{0.45} X^{0.13}}{\rho_l^{0.45} D^{0.85}} \quad (6)$$

with

$$S = Re^{0.1} Fr^{0.45} \left(\frac{D}{d_p}\right)^{0.2} X^{0.13} \quad (7)$$

where d_{p0} is the particle diameter, ν is the viscosity of the liquid, g is the gravitational acceleration, and $\Delta \rho$ is the difference between the particles and the liquid density. X stands for the initial solids mass fraction in %, ρ_l is the density of the liquid, and D represents the impeller diameter. The dimensionless number S is a function of the impeller type as well as of D/T and C/T .

Homogenization. During dissolution the concentration c (and therefore the viscosity) of the solution changes. The concentration (as well as the viscosity) field in the tank needs to be homogenized by additional agitation. In order to quantify

the homogenization process, a uniformity index is defined as

$$I_u = 1 - 0.5 \cdot \sum_j \frac{V_j}{V_{tot}} \left| \frac{c_j - c_{mean}}{c_{mean}} \right| \quad (8)$$

V_j , V_{tot} , c_j , and c_{mean} are the cell volume of the computational cell j , the total volume of the domain, the local, and the averaged concentration over the entire volume, respectively.

Scale-up. The scale-up of solid–liquid mixing processes is complex since various effects need to be balanced simultaneously.² In the case of solids feeding, additional variables enter the picture. Thus, the objectives of the scale-up need to be determined *a priori*. These include for example identical blend times, identical uniformity of the solid distribution in the vessel, identical dissolution times, or equal volumetric power input or torque in the small-scale and large-scale system. Often, scale-up with respect to one parameter is not feasible. For example, if the blend time must be the same in the small- and large-scale vessels, the rotation rate must be the same in both vessels, leading to a dramatic increase in the power input. Scale-up based on the same power input (or torque) per volume leads to increased blend and/or dissolution times. If the dissolution time needs to be the same, the local mass transfer coefficient, which is a function of the turbulent spectrum, needs to be identical for the small- and large-scale vessels. However, caution must be exercised: if the feeding rate per volume is the same, wetting and dissolution of the solid at the surface may become limiting, as the free surface scales with the T^2 while the addition rate scales needs to scale with T^3 .

METHODS

CFD Simulation. First, a transient, incompressible, single-phase model was implemented, which was then validated via PIV. For solving the continuity and the momentum equations, the CFD code FIRE release 2009.2 was used.⁴³ Since the algorithm and the numerical discretization method are well-known, a detailed description is omitted. For details refer to Patankar and Spalding.⁴⁴ Turbulent effects were modeled by a k - ζ - f turbulence model,³⁸ a general low-Reynolds-number eddy-viscosity model based on Durbin's elliptic relaxation concept.⁴⁵ Here k is the turbulence kinetic energy, ζ is the normalized velocity scale ratio, and f is the elliptic relaxation function. The formulation is similar to the standard k - ε model, though it includes nonlocal pressure-strain effects and near-wall turbulence anisotropy. In this model the eddy viscosity ν_t is related to the velocity scale \bar{v}^2 by means of the velocity scale ratio as

$$\nu_t = C_\mu \zeta \frac{k^2}{\varepsilon} \quad (9)$$

with

$$\zeta = \bar{v}^2 / k \quad (10)$$

C_μ is a model coefficient, and ε is the dissipation rate of the turbulence kinetic energy. The advantage of the k - ζ - f model is that it does not require the adoption of wall functions, since velocity scale \bar{v}^2 describes the velocity fluctuations normal to the main streamlines and represents the turbulent damping close to the wall. In addition to the standard k and ε -equations, the transport

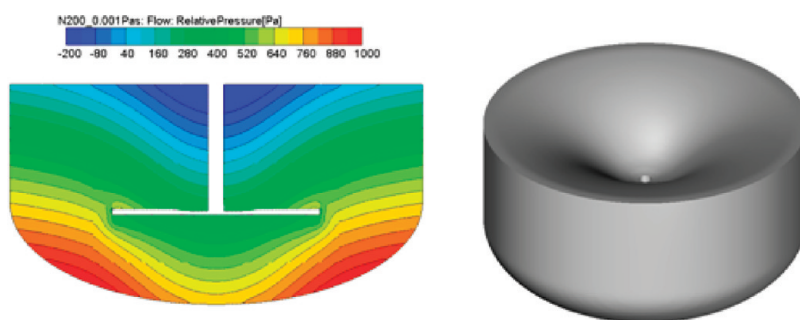


Figure 4. Left: pressure distribution of the closed surface simulation indicates size and shape of the vortex. Right: final mesh geometry of the vortex surface.

equation for ζ is solved

$$\frac{D\zeta}{Dt} = f - \frac{\zeta}{k} P_k + \frac{\partial}{\partial x_j} \left[\left(\nu + \frac{\nu_t}{\sigma_k} \right) \frac{\partial \zeta}{\partial x_j} \right] \quad (11)$$

An elliptic equation of the Helmholtz type for the relaxation function f depending on turbulent time and length scales is solved as well⁴⁵

$$f = L^2 \frac{\partial^2 f}{\partial x_j \partial x_j} - \frac{1}{T_t} \left(C_1 - 1 + C_2 \frac{P}{\varepsilon} \right) \left(\zeta - \frac{2}{3} \right) \quad (12)$$

The turbulent time scale T_t and length scale L are calculated as

$$T_t = \max \left(\frac{k}{\varepsilon}, 6 \sqrt{\frac{\nu}{\varepsilon}} \right) \quad (13)$$

$$L = C_L \max \left(\frac{k^{3/2}}{\varepsilon}, C_\eta \frac{\nu^{3/4}}{\varepsilon^{1/4}} \right) \quad (14)$$

In order to describe the rotation of the impeller, different models are used,² i.e., the Multiple Reference Frames model (MRF) and the Sliding Mesh model (SM). MRF is a simple steady-state model in which the mesh domain is divided in two or more meshes. A rotating frame is used for the region containing the impeller, while a stationary frame is used for the nonmoving mesh. The model solves the momentum equations for the rotating frame including the Coriolis force. Both the impeller in the rotating frame and the tank walls in the stationary frame are at rest. The impeller itself is assumed to be static for this type of calculation, which also means that the orientation of the impeller blades versus stationary elements within the tank does not change. At the MRF interface between the rotor and the stator domain, the flow information is transferred during the solution process.

Like the MRF model, the SM model requires the mesh to be separated into a rotor and a stator meshes for the domain including the impeller and the domain including the tank walls, respectively. Under the SM model approach, the equations are solved in a transient (time-dependent) mode. The rotor mesh physically moves during the solution, not continually but in small, discrete steps. After each time-step, i.e., after each motion of the rotor mesh, the RANS and the mass continuity equations are solved iteratively until convergence is reached. Information of the rotor mesh is transferred through the interface to the stator mesh and vice versa. In our work the SM model is used for

Table 1. Parameters of the Simulated Mixing Systems

liquid	2.8 L water; dynamic viscosity $\mu = 0.001$ Pa s
tank	cylindrical shaped tank with an elliptical-shaped bottom tank diameter $T = 0.2$ m
impeller	pitched blade turbine (BPT) in up-pumping mode and center position 4 blades
	impeller diameter $D = 0.1$ m
	impeller clearance from the bottom $C = 0.045$ m
	impeller speed $N = 200$ rpm

transient calculations, allowing the simulation of a (transient) dissolution process.

In order to compute the shape of the surface, a single-phase approach was used comparable to the method presented by Ciofalo et al.¹⁴ The adopted iterative method involves the following steps:

- A steady-state simulation of the stirred tank is performed with a closed surface employing the MRF impeller model.
- The surface pressure distribution is computed.
- An isobaric surface is assumed to be the real free surface.
- The lowest pressure isobar surface that covers the entire diameter of the tank is selected as the new liquid surface.
- The flow domain of the tank is remeshed for the new surface.
- Recheck can be done by performing another steady-state calculation.

As indicated above, the vortex depth will vary when fluid and process parameters (viscosity, stirring speed, etc.) change. Thus, different stirrer rotation rates lead to different vortex depths, and, as a consequence, different simulation meshes are required. The results for a typical case (water) are shown in Figure 4. The parameters used for the simulation are summarized in Table 1.

For a typical case (same as Figure 4) simulations were carried out. The comparison of the results obtained from the CFD simulation and the Zlokarnik equation (eq 5) for propeller type impellers is presented in Table 2. As can be seen, the agreement is very good.

While dissolution and homogenization take place, the viscosity of the solution increases. Thus, the Re number decreases, affecting the vortex depth. In this work, simulations for specific process stages were performed which the viscosity and the vortex depth were treated as constant. Furthermore, for our simulations we assumed an isothermal system.

Mixing Calculations. In the mixing simulations the SM model was used for the calculation of the impeller movement. After a certain number of rotations a quasi-steady state (QSS) was reached, as observed by Bakker et al.⁷ In order to quantify the approach of the QSS, three values were computed, i.e., (1) the volume-averaged total velocity, (2) the volume-averaged tangential velocity, and (3) the torque acting on the impeller. The number of revolutions required to achieve the periodic quasi-steady state typically increases with the Re number. Figure 5 shows that for a low Reynolds number of Re = 400 (transitional regime), a few revolutions were sufficient, while for a high Reynolds number of Re = 33,300 (turbulent regime) even 30 revolutions were not enough to approach the QSS, as the averaged tangential velocity was not constant after 30 revolutions.

In order to accelerate the simulations, a preliminary steady-state MRF simulation was performed to estimate the velocity field, which subsequently was used to initialize the transient sliding mesh calculation that is required for calculations of mixing and the dissolution processes. This led to constant volume averaged tangential velocities after approximately 20 revolutions for the same system with Re = 33,000.

The torque as shown in Figure 6 was computed for several cases and agreed well with literature values. For example, for a Reynolds number of 33,300 a power number Ne for a pitched blade turbine in an unbaffled tank of 0.73 was obtained, which agrees well with the power number 0.7 stated in the literature.⁴⁶

Solid particles were tracked via the Lagrangian DPM (Discrete Particle Method) approach, also known as the Lagrangian Monte Carlo method, which was first proposed by Dukowicz.⁴⁷ The basic concept of this method is to track the statistical parcel paths of real particles in physical, velocity, and particle-diameter space. Submodels for drag, particle/wall interaction, dissolution, and turbulent dispersion were included in our simulations. In the DPM method each physical phenomenon occurring in a parcel,

e.g., dissolution, directly applies to all the particles in the parcel. This allows a drastic reduction in the computational effort.

In the simulations the effects of collision between parcels were neglected. This is a valid assumption as the volume fraction of the bulk material is low. Mass and momentum balance equations are solved for each parcel *i*. The continuity equation for each parcel can be written as

$$\frac{dm_{ip}}{dt} = -\dot{m}_{iD} \quad (15)$$

where the term on the right side represents the mass source due to dissolution. In the Lagrangian DPM, the momentum equation, i.e., Newton's second law, is directly integrated over time for each parcel

$$m_{ip} \frac{d\vec{u}_{ip}}{dt} = \vec{F}_{i,d} + \vec{F}_{i,g} + \vec{F}_{i,p} \quad (16)$$

The terms on the right side of eq 16 are the drag force $F_{i,d}$, the gravity and buoyancy force $F_{i,g}$, and the pressure force $F_{i,p}$. The drag force acting on the particles is calculated as

$$\vec{F}_{i,d} = \frac{1}{2} \rho_l A_p C_D |\vec{u}_{rel}| \vec{u}_{rel} \quad (17)$$

where ρ_l is the liquid density, A_p is the cross-sectional area of the particles, and u_{rel} is the relative velocity between the liquid phase and the parcel. The term C_D represents the drag coefficient for a single sphere and is modeled in our work according to the formulation of Schiller and Naumann⁴⁸

$$C_D = \begin{cases} \frac{24}{Re_p} (1 + 0.15 Re_p^{0.687}), & Re_p < 10^3 \\ 0.44, & Re_p \geq 10^3 \end{cases} \quad (18)$$

Table 2. Comparison of Vortex Depth h' Calculated with eq 5 and the Result Obtained by CFD Simulations

	h' by (eq 5)	h' by CFD
$T = 0.2$ m	$h' = 0.027$ m	$h' = 0.029$ m
$T/D = 2$		
$S = 0.063$ m		
$N = 200$ rpm		
$\mu = 0.001$ Pas		
$Ga = 9.81 \times 10^9$		
$Fr = 0.113$		

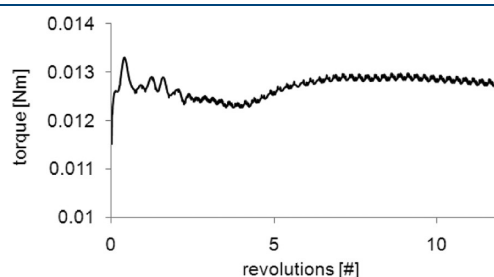


Figure 6. Torque acting on the impeller; Re = 33,000; parameter summarized in Table 1.

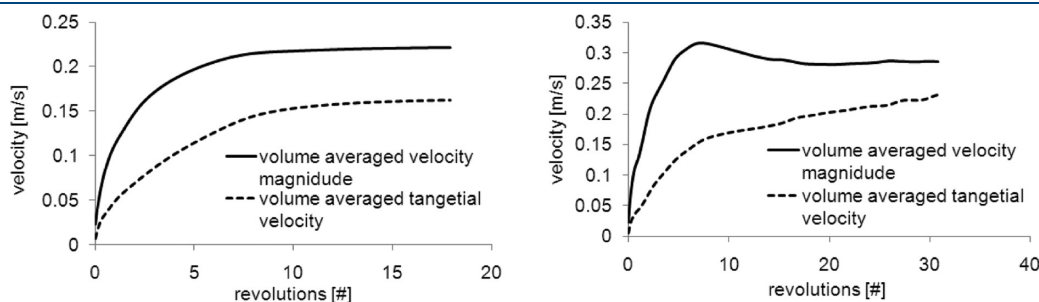


Figure 5. Sliding mesh calculation: mean absolute and tangential velocities vs impeller revolutions for Re = 400 (left) and Re = 33,300 (right).

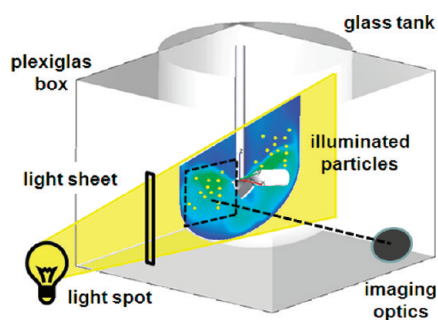


Figure 7. Basic setup for PIV measurements. The tracer particles in the stirred glass tank are made visible by an incident light sheet and are registered by a CCD camera oriented normally to the light plane.

Here the particle Reynolds number Re_p is defined as

$$Re_p = \frac{\rho_l |\vec{u}_{rel}| D_p}{\mu_l} \quad (19)$$

The gravity and buoyancy force $F_{i,g}$ and the pressure force $F_{i,p}$ are given by

$$F_{i,g} = V_p \cdot (\rho_p - \rho_l) g_i \quad (20)$$

$$F_{i,p} = V_p \cdot \nabla p \quad (21)$$

where g_i is the gravitational acceleration. ρ_p and ρ_l are the densities of the particles and the liquid, respectively, V_p is the volume of the particle, and ∇p is the pressure gradient.

Turbulent Dispersion Model. In a stirred tank particles are lifted from the tank bottom by a combination of drag and lift forces and by the bursts of eddies generated by the turbulent flow at the tank wall. In order to account for these additional effects, a turbulent dispersion model based on the work of Gosman and Ioannidis was implemented. Here, the particle path is determined similar to a random walk through a turbulent eddy. The interaction time of the particle within an individual eddy is estimated based on two criteria, i.e., the turbulent eddy lifetime and the time required for the particle to cross the eddy.⁴⁹ In our eddy interaction model,⁵⁰ the effects of turbulence on the particles are modeled by adding a fluctuating velocity u_i' to the main particle velocity. Assuming isotropic turbulence, the components of the particle fluctuating velocity u_i' is randomly determined from a Gaussian distribution with a standard deviation $\sigma = (2/3 k)^{1/2}$, where k is the turbulence kinetic energy of the fluid at the particle location

$$u_i' = \left(\frac{2}{3} k \right)^{1/2} \text{sign}(2R_i - 1) \cdot \text{erf}^{-1}(2R_i - 1) \quad (22)$$

R_i is a random number in the range of [0 to 1] for each vector component i , and erf^{-1} is the inverse Gauss function. The fluctuation velocity u_i' is chosen as a piecewise constant function of time and is updated each turbulence correlation time t_{turb} , defined as the minimum of the eddy break-up time and the time for the particle to traverse an eddy

$$t_{\text{turb}} = \min \left(C_\tau \frac{k}{\varepsilon}, C_1 \frac{k^{3/2}}{\varepsilon} \cdot \frac{1}{|u_l + u' - u_d|} \right) \quad (23)$$

here $C_\tau = 1.0$ and $C_1 = 0.16432$ are model constants.

If the computational time step δt is greater than the turbulence correlation time t_{turb} , the Lagrangian integration time step is reduced to t_{turb} .

Mass Transfer. The mass transfer rate, and thus, the dissolution rate is a function of the equilibrium solubility of the solute, the specific surface of the particles, the concentration of the dissolved material, the diffusion constant in the liquid phase, and the relative velocities of the particle and the fluid. It is well-known that the dissolution rate in tanks first increases rapidly with stirring rate until homogeneous suspension is reached. From then on the dissolution rate reaches a plateau. In our work, the mass transfer rate is described by a Frössling type equation developed by Nienow and Miles.⁵¹ The dissolution rate \dot{m}_{ip} (eq 24) of one particle is a function of the molar mass M_G , the diffusion coefficient D_A , the particle surface A , and diameter d_p , the gradient between the local liquid concentration c_∞ , and the saturation concentration c_s in the specified liquid

$$\dot{m}_{ip} = M_G \frac{Sh \cdot D_A}{d_p} A (c_s - c_\infty) \quad (24)$$

The Sherwood number (eq 25) is a function of Re and Schmidt numbers

$$Sh = 2 + 0.552 \sqrt{Re} Sc^{1/3} \quad (25)$$

For quantifying the homogeneity of the mixture three values are computed, i.e., (1) the undissolved mass in the system, (2) the dissolved mass, and (3) the uniformity index for mass concentration (eq 8).

Conservation Equation for Concentration (scalars). The conservation equation for mass using Fick's law for binary diffusion is

$$\frac{\partial}{\partial t} \rho c + \frac{\partial}{\partial x_j} (\rho u_j) c = \frac{\partial}{\partial x_j} \left(D_A \frac{\partial c}{\partial x_j} \right) + \rho S_c \quad (26)$$

where D_A is the diffusion coefficient, c is the local scalar concentration, u_j is the velocity component, ρ is the local liquid density, and S_c is the local source of scalar.

Particle Image Velocimetry. PIV is a well-known optical method for analyzing the fluid flow by capturing the movement of small tracer particles.⁹ This method was utilized to validate single-phase CFD simulations. The PIV technique involves a sufficiently large amount of particles suspended in a fluid that are homogeneously distributed and that does not interfere with each other or change the flow properties. Seed particles are acting as tracers and can be used to determine the fluid velocity at each point of the fluid. The principle setup of the PIV measurements is shown in Figure 7. At the probing point, the fluid is illuminated with a pulsed laser. The light reflected by the particles is captured with a CCD (Charged-Coupled-Device) camera. By comparing the images of different points in time, the displacements of the particles (or particle assemblies) can be calculated. Our calculation was performed via a statistical cross-correlation technique, which calculates the similarities between two subimages at two time instances. Essentially, the intensity distribution of the first subimage and the second displaced subimage is multiplied and the sum of all pixels is calculated. This sum is evaluated as a function of different displacements of the second subimage. When the sum reaches a maximum, the correct direction and amplitude of the displacement vector is found. The velocity is then calculated by dividing the displacement by the time span

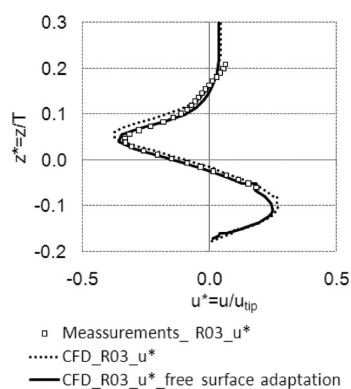


Figure 8. Quantitative comparison between measurements and simulation. Dimensionless radial velocity u^* vs z^* (dimensionless coordinate) at $r^* = -0.3$.

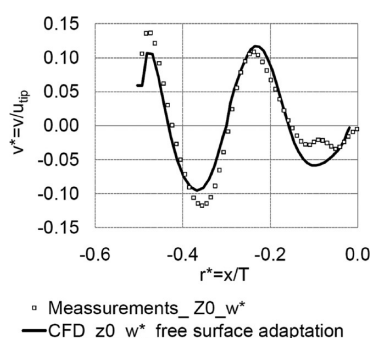


Figure 9. Quantitative comparison between PIV measurements and simulation. Dimensionless axial velocity v^* vs r^* (dimensionless coordinate) at $z^* = 0$.

between the images. Obviously, higher resolution in time and space lead to a higher accuracy.

To speed up postprocessing, the images are divided into segments. For each segment, the displacement is calculated separately, leading to a 2D vector field for each time step.

RESULTS AND DISCUSSION

In the first part of this section, the simulation model is tested and validated via PIV measurements. The second part presents results from the study of powder dissolution in a stirred tank.

Comparison of PIV Data with CFD Results. The tank used for validation case was an unbaffled glass vessel with an elliptical bottom, with a diameter of $T = 0.2$ m and a liquid height of 0.108 m. The impeller was a pitched blade turbine (BPT) with a diameter $D = T/2$ placed in the center with a bottom clearance of $C = 0.45D$. The liquid phase was a 40 w% solution of PEG 6000 in water. The dynamic viscosity was $\eta = 0.086$ Pa s and the density $\rho = 1100$ kg/m³. The impeller speed was $N = 200$ rpm, and the corresponding Re number was $Re = 390$. Thus, the system operated in the transitional regime.

A time-averaging procedure was used for the simulations, as the PIV measurements were averaged over time (Figure 8).

Figure 8 shows PIV results (square dots) in comparison with those obtained by simulations with a closed surface (dashed line) and with a surface vortex (solid line). The lines represent the radial velocities along the vertical line at the radius $r^* = -0.3$. The velocities are normalized by the tip speed. The measurement

Table 3. Settings of the Investigated Mixing System: Basic Configuration

parameters	values
tank type	unbaffled glass with elliptical bottom
tank diameter	$T = 0.2$ m
liquid height	$H = 0.108$ m
tank volume	2.8 L
impeller type	pitched blade
impeller diameter	$D = T/2$
impeller position	center
clearance between impeller and tank bottom	$C = 0.45 D$
continuous phase	water
dynamic viscosity	$\eta = 10^{-3}$ Pa s
density	$\rho = 10^3$ kg/m ³
impeller speed	$N = 200$ rpm
Re number	$Re = 33,300$
particles that represent the bulk powder	spheres
start diameter	$d_p = 0.5 \times 10^{-3}$ m
density	$\rho_p = 1.08 \times 10^3$ kg/m ³
diffusivity	$D_A = 1.15 \times 10^{-10}$ m ² /s (PEG 6000 in water)
feeding rate and time	5×10^{-4} kg/s for 1 s
feeding area	circle with 5 cm in diameter below the impeller

results are constrained in height because the intensity of the light sheet used for the PIV measurements was limited. As can be seen, a very good agreement between the simulation and experimental results was obtained. The results of the free-surface-adaptation simulations agree even better with the PIV measurements.

Figure 9 shows a comparison between the axial velocity v^* for the PIV measurements (squared dots) and the simulation results (solid) along a horizontal line $z^* = 0$. A good agreement between simulations and experiments can be seen. Similarly, a good agreement was obtained for all other measured velocities in the tank.

Powder Dissolution and Mixing. The parameters for the simulations are summarized in Table 3.

The above settings represent the base case B of our simulation study. One parameter was changed for each simulation. The variation star is shown in Figure 10 below.

The following variations were studied:

- Variation 1 - stirring speed. The stirring speed of the impeller was set to $N = 100$ rpm. Thus, the Re number was reduced to $Re = 16,650$.
- Variation 2 - rotation direction of the impeller. The impeller rotated counterclockwise at the speed of 200 rpm.
- Variation 3 - feeding position I. The feeding area is on the liquid surface (see Figure 11).
- Variation 4 - feeding position II. The feeding position is close to the tank wall (see Figure 11).
- Variation 5 - particle size. The size of the feeding particles was changed from 500 to 100 μ m.
- Variation 6 - dynamic viscosity. The dynamic viscosity of the solution was set to 0.085 Pa s. Thus, the Re number was reduced to $Re = 400$.

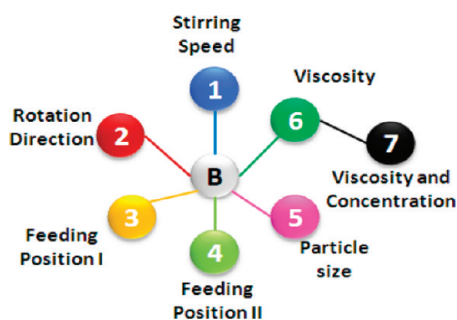


Figure 10. Simulation variation star.

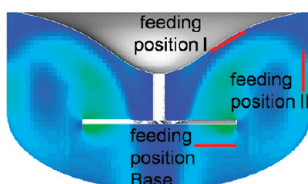


Figure 11. Different feeding positions; red lines indicate the three feeding positions of the base case position, position I for variation 3 and feeding position II for variation 4; predicted flow patterns in the vessel with an up-pumping pitched blade turbine at 200 rpm. Blue and green areas indicate low and high velocities, respectively.

- Variation 7 - dynamic viscosity and mass concentration. Both the dynamic viscosity and the mass concentration were changed to 0.085 Pa s and 40 w%, respectively.

Flow Patterns. Based on the parameters from the variation star four different flow patterns are obtained and shown in Figure 12. The absolute velocity is indicated by the color code. As predicted by eq 5, for lower viscosities and higher impeller speeds, the vortex depth is higher.

Variation 1 (Figure 12b) shows a lower velocity than the base case as the stirrer speed has been reduced by 50%. Thus, the mixing time is expected to increase. In case of variation 2 (Figure 12c) the fluid is pumped downward. Compared to the base case smaller recirculation zones close to the fluid free surface exist. The vortex is a little sharper, while the vortex depth was not changed by changing the rotation direction of the impeller. Compared to the base case, the flow pattern most radically changes for variations 6 and 7 (Figure 12d), as the viscosity is increased. As can be clearly seen, velocity gradients are localized close to the impeller, thus leading to poor mixing in zones far from the impeller.

Dissolution. Next, the effect of the flow patterns on the dissolution behavior of solid particles was investigated. For the simulations it was assumed that 0.5 g of powder (PEG 6000) is fed over a time span of 1 s (about 3.3 impeller revolutions in the base case). In the computations the feeding process was started when the quasi-steady state was achieved. Figure 13 shows the dissolved mass vs time for the cases presented above.

The results presented in Figure 13 indicate that variations 1, 5, and 7 lead to a significant and variation 6 leads to a small change in the dissolution kinetics over time. Reducing the impeller rotation speed by 50% (variation 1) lead to a decrease in the dissolution rate and an increase in the dissolution time (defined as the time it takes to dissolve 99% of the solid) from 6.4 s to 8.8 s. For variation 5 (a particle size of one-fifth of the basic particle

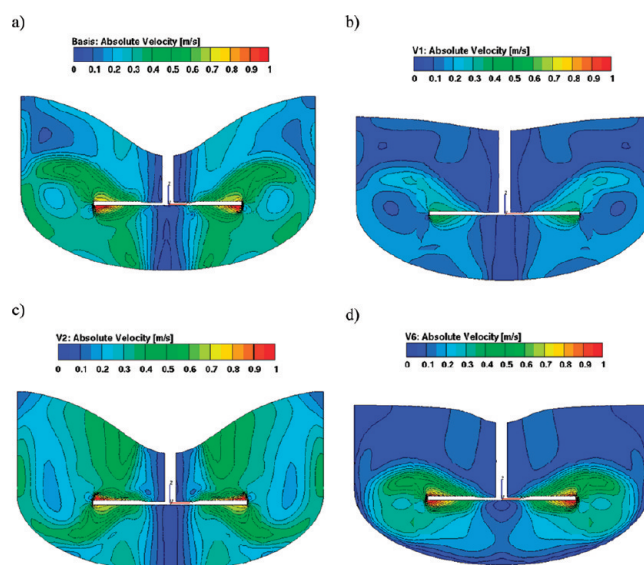


Figure 12. Comparison of flow patterns of the different variations: (a) base case, V3, V4, and V5, (b) V1, (c) V2, and (d) V6 and V7.

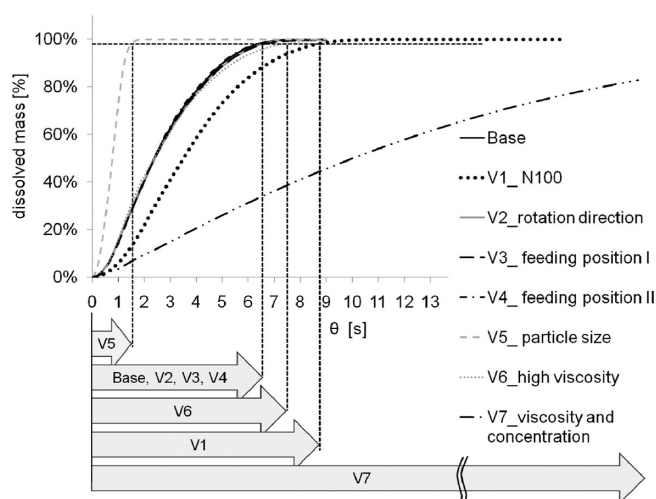


Figure 13. Dissolved mass vs time θ for the base case and variations V1–7. Variations V1, V5, and V7 lead to significant changes of the dissolved mass over time.

size) the dissolution process was considerably faster, and the dissolution time was reduced by more than 75%, i.e., 1.5 s vs 6.4 s. Simultaneously increasing the dynamic viscosity and the mass concentration of the solution from 0 w% to 40 w%, which is close to the saturation concentration of PEG 6000 in water, slowed down the dissolution process most significantly. The dissolution time for variation 7 is longer than 21 s. The change of the dynamic viscosity from 0.001 Pa s to 0.085 Pa s increases the dissolution time from 6.4 to 7.5 s. Interestingly, the dissolution kinetics were not significantly affected by the direction of rotation and the feeding position especially for the small volume tanks analyzed in this study.

A similar trend can be observed when examining the undissolved mass in the system (Figure 14). For variation 5 (reduced particle diameter), the solid mass disappeared nearly three times faster than for the base case. The main reason for this is the

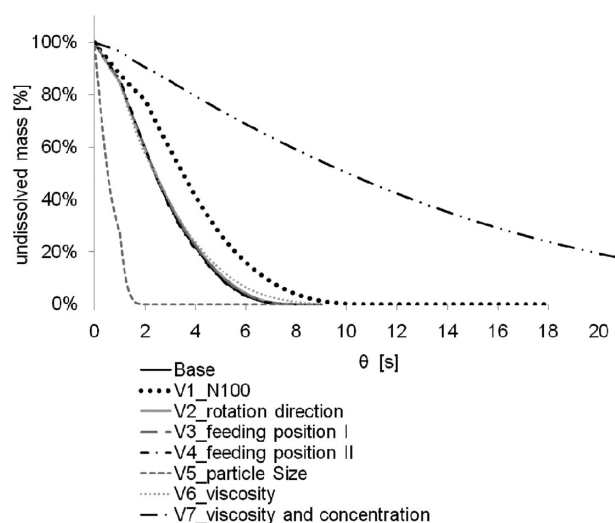


Figure 14. Undissolved mass vs time for the base case and variations 1–7.

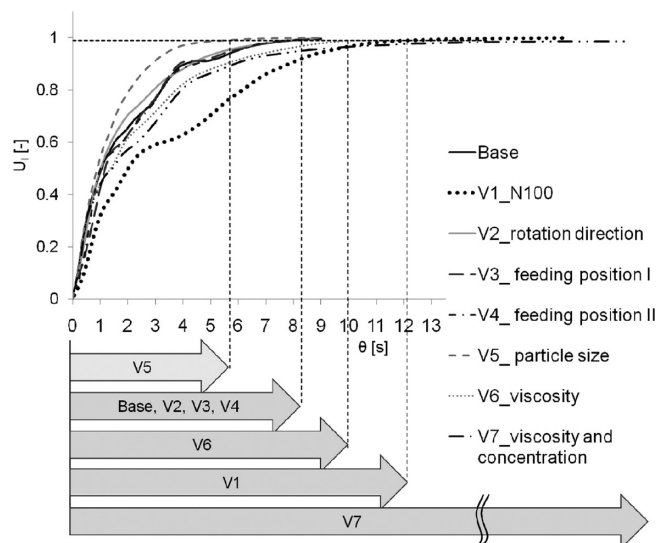


Figure 15. Uniformity index vs time for the base case and variations 1–7.

increased particle surface-to-volume ratio. As mentioned above, the particles were fed during the time span that the impeller takes for 1200° . Therefore, the feeding time was 1 s for the base case and 2 s for the variation V1. The end of the feeding time is well-identifiable by the change in slope in Figure 14.

Mixing. The mixing time θ is defined as the time it takes to reach a uniformity index of 0.99. Figure 15 shows the uniformity index as a function of mixing time. Interestingly, while the dissolution process for variation 5 (small particles) is about four times faster than for the base case, the mixing time is only 1.5 times shorter. This can be attributed to the fact that the mixing time and dissolution time are affected by different effects. Dissolution is strongly influenced by the specific surface area of the particles and to a lesser extent by the local liquid-phase flow. Macro-mixing, in contrast, is affected mainly by changes of the Re number. As the Re number is the same for the base case and variation 5, the effect on the mixing time is small. The mixing time for variation 1 is approximately 50% longer than that for the

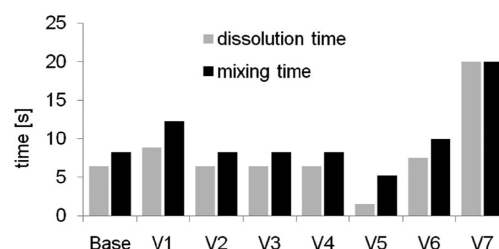


Figure 16. Mixing and dissolution times for all variations.

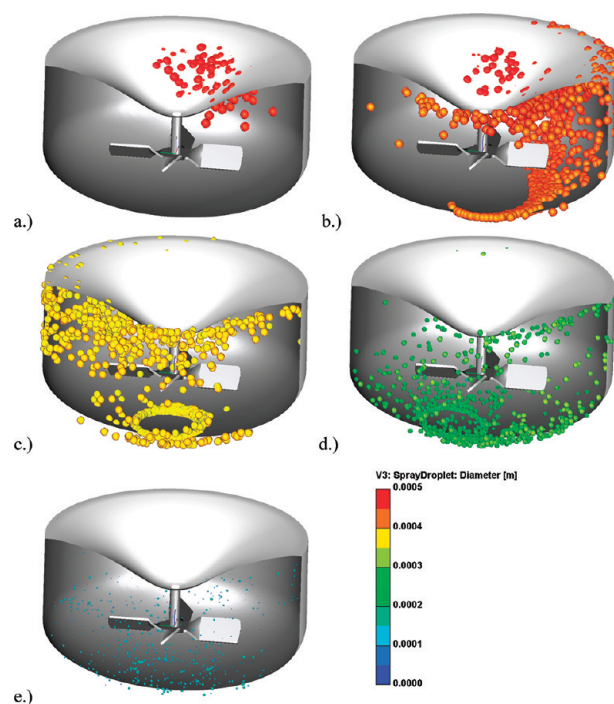


Figure 17. Particle flow V3-feeding position at vortex surface: a) revolution 1 after start of feeding, b) revolution 3.3 (=feeding end), c) revolution 8.3, d) revolution 15.8, and e) revolution 24.5. Color bar signifies particle size.

base case, illustrating that stirring does not have a significant impact on the dissolution (see Figure 16) but influences mixing significantly. Both the dissolution and the mixing time for variation 6 are approximately 20% longer than that of the base case. In this case the change of the viscosity leads to a more localized flow pattern and, therefore, to poor up-to-down mixing. Mixing time for variation 7 is significantly increased, as the dissolution time is much longer, in addition to the poorer mixing in the case of the high-viscosity fluid. Moreover, changing the rotation direction of the impeller, which leads to a change in the pumping direction of the impeller (i.e., up-pumping versus down-pumping for the base system and V2, respectively), had no major effect on the dissolution and mixing.

In order to investigate the impact of the feeding position on the dissolution time, three different feeding positions were studied: the base case position under the impeller, at the vortex surface (V3) and near the wall (V4), as shown in Figure 11. As the figures above clearly showed, the variation of the feeding position (V3–4) had no significant impact on the dissolution and mixing. However, this is only true if wetting effects at the free

surface are negligible. The reason for this behavior is that the dispersion time (i.e., the time used to disperse the particles in the vessel) is more than one magnitude shorter than the dissolution time.¹⁸

A summary of the dissolution and mixing results is shown in Figure 16. As can be seen, mixing times are always (slightly) longer than dissolution times which is expected as complete homogenization can be achieved only after complete dissolution. In some cases, however, the difference between dissolution and mixing is significant, for example in the case of small particles, as in this case dissolution is very fast, faster than mixing in the tank.

Particle Suspension. Particle suspension is a critical factor in the dissolution of particles, as particles at the bottom may agglomerate, especially if particles are sticky. Thus, it is important to operate the tank in a regime where complete suspension of the particles is achieved. In this study, particle suspension has been investigated as well. Figure 17(a-e) shows snapshots of particles for variation 3, i.e., particles are fed at the vortex surface. Particle size and color code are directly proportional to the real particle size. It can be seen that the particle size decreased with time (pictures a-e). The rotation speed of the impeller was approximately twice as high as suggested by the Zwietering correlation (eq 6), i.e., particles remain just suspended. Nevertheless, many

particles are located in the region below the impeller, near to the tank bottom (see Figure 17 b-c), due to the flow behavior inside the unbaffled reactor. In the bottom region, the flow is mainly rotating. It tends to retain the particles in a big vertical eddy generated by the rotating impeller.

Figure 18 for variation 3 shows trajectories of a typical particle that is fed at the surface. Every second the color of the trajectory changes. It can be seen that the residence time on the tank bottom is less than 1 s, as suggested by the Zwietering criterion. Thus, the model correctly predicts the suspension in the tank.

Tank Scale-up. Most of the known scaling-up criteria are based on geometrical similarity. For constant liquid properties and relatively small scaling-up ratios it is a good choice to keep the power consumption per volume constant (i.e., $N_1^3 D_1^2 = N_2^3 D_2^2$) especially for turbulent flows. Another approach is to keep the tip speed constant (i.e., $N_1 D_1 = N_2 D_2$). A third criterion is the approach that keeps the flow regime similar ($Re = \text{const.}$, i.e., $N_1 D_1^2 = N_2 D_2^2$).

When scaling-up a solid–liquid mixing system, different objectives need to be met. For example, the uniformity level of the suspended solid should be equal. Alternatively, the time to achieve complete dissolution and the power needed per mixing volume may be required to be equal. Often the objective is to preserve the Batchelor scale in order to keep mass-transfer-limited

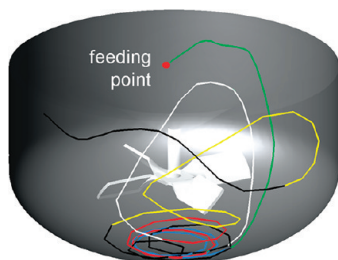


Figure 18. Particle trajectory of a typical particle fed at the vortex surface (V3). Color of the trajectory changes every second.

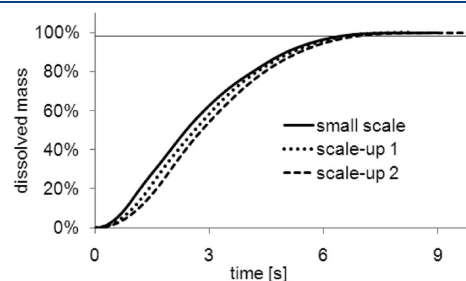


Figure 19. Dissolved mass vs time for the three cases.

Table 4. System Parameter: Small Scale, Scale-up 1, and Scale-up 2

	small scale	scale-up 1	scale-up 2	
tank diameter	0.2	0.4	0.6	[m]
impeller diameter	0.1	0.2	0.3	[m]
liquid height	0.108	0.216	0.324	[m]
clearance	0.045	0.09	0.135	[m]
liquid volume	2.8	23.3	78.8	[liter]
impeller speed	200	126	96	[rpm]
density	1000	1000	1000	[kg/m ³]
dyn. viscosity	0.001	0.001	0.001	[Pas]
Newton number	0.73	0.73	0.73	[-]
filling height above impeller	0.063	0.126	0.189	[m]
kinetic viscosity	0.000001	0.000001	0.000001	[m ² /s]
power consumption	0.27	2.16	7.27	[W]
diameter ratio	2	2	2	[-]
specific liquid height	0.54	0.54	0.54	[-]
specific clearance	0.45	0.45	0.45	[-]
Reynolds number	33333	84000	144000	[-]
Froude number	0.113	0.090	0.078	[-]
Galilei number	9.81×10^9	7.85×10^{10}	2.6487×10^{11}	[-]
$N^3 D^2$ (Batchelor scale)	0.370	0.370	0.369	[m ² /s ³]
specific power consumption	97	93	92	[W/m ³]

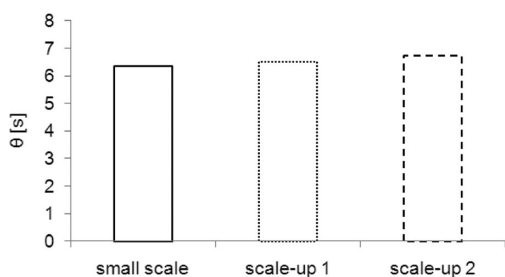


Figure 20. Dissolution time for the three cases.

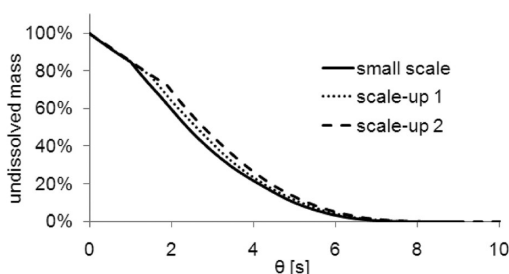


Figure 21. Undissolved powder mass vs time for the basic and the scale-up V1 and V2 variations.

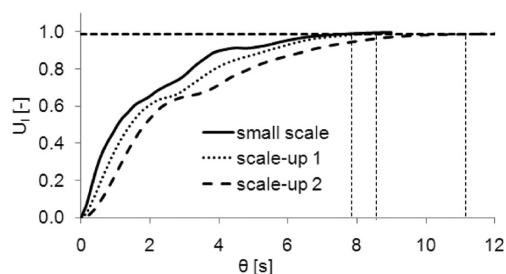


Figure 22. Uniformity index vs time for all three cases.

or mixing-limited reaction kinetics constant.² The Batchelor scale λ_B describes the size of a scalar droplet that will diffuse within the same time it takes the energy in an eddy of size η (Kolmogorov scale) to dissipate

$$\lambda_B = \left(\frac{\nu D_{AB}^2}{N_P N^3 D^2} \right)^{1/4} \quad (27)$$

Here ν , D_{AB} , N_P , N , and D are the kinematic viscosity, the mass diffusivity, the power number, the impeller speed, and the impeller diameter, respectively. Preserving λ_B means for constant liquid properties

$$N^3 D^2 = \text{constant} \quad (28)$$

For the scale-up study that is shown below, the Batchelor scale was kept constant in order to obtain similar dissolution behavior of the particles. The mass fed was adjusted to yield the same final concentration. The following cases were studied:

- Scale-up 1: scale-up by factor 2. The stirrer speed that keeps the Batchelor scale constant is 126 rpm. The Re number increased to $Re = 84,000$

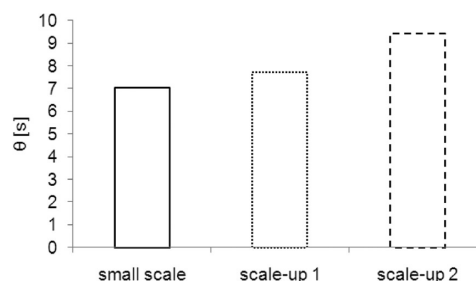


Figure 23. Macro mixing time for all three cases.

- Scale-up 2: scale-up by factor 3. The stirrer speed for the constant Batchelor scale is 96 rpm. The Re number increased to $Re = 144,000$

In Table 4 the parameters of the small-scale tank and the scaled-up systems are summarized.

The $N^3 D^2$ -values of the three systems were considered to be constant for preserving the Batchelor scale. Therefore, the dissolution time can be expected to be constant.

The dissolved mass as a function of time is shown in Figure 19 for the above-mentioned three cases. For the small scale system with a starting volume of 2.8 L the mass of the bulk powder fed to the vessel was 0.5 g. The cases 'scale-up 1' and 'scale-up 2' have a starting volume of 23.3 L and 78.8 L, respectively. Thus, the total powder mass fed was 4.1 and 14 g for scale-up 1 and 2, respectively. As can be seen in Figure 19, the dissolution times are essentially the same. The same finding is shown in Figure 20, which presents the dissolution time after which 98% of the particle mass is dissolved in the three cases.

Figure 21 shows the undissolved mass vs time for the three cases. The mass was fed over the time span the impeller takes for 1200° , which equals 1 s in the Basic System. Therefore, the feeding period is 1.59 and 2.08 s for the variations 1 and 2, respectively. The end of the feeding period is clearly indicated by a sharp bend in Figure 21. Still, the dissolution time can be considered constant.

The uniformity index vs time shown in Figure 22 indicates that in the large-scale system the homogenization takes considerably longer than for the small scale system. The mixing time is known to decrease directly proportionally to the stirrer speed for $Re = 10^3 - 10^4$. When $Re > 10^5$ the mixing time increases with the square of the impeller diameter.¹ Figure 23 shows that the mixing time for all three cases confirms this trend.

CONCLUSIONS AND OUTLOOK

In this paper we present a simulation method for studying mixing and dissolution processes of solids in low to moderately viscous liquids. Mixing and dissolution was performed in an unbaffled agitated tank, where the flow was forced by a pitched-blade turbine. For validation purposes, the simulation results were compared to PIV measurements. A method for the description of the vortex formation, especially in highly turbulent systems in an unbaffled tank with the impeller placed in center position, was presented. The simulation of the dissolution process of powder particles was carried out by tracking the movement of solid particles with the Lagrangian DPM approach and, additionally, by describing the dissolution of the particles as a function of local Reynolds and Schmidt numbers. Finally, the presented method was utilized in a parameter-variation and a

scale-up study. The variation study helped to identify the best combinations of the stirring equipment and stirring parameters. In the scale-up study, the dissolution time was supposed to be kept constant.

In industry, often only small amounts of product are available for testing and process development. Therefore, “in-silico” techniques are a promising and effective way of optimizing a production process. As other numerical methods our approach includes some assumptions and constraints. These can, however, be relaxed during future studies. In summary, the numerical approach can

- accurately predict the flow in an agitated unbaffled tank.
- describe vortex formation by implementing an iterative surface correction method.
- simulate the flow of particles (i.e., suspensions) of low concentration.
- model the dissolution process and the mixing process of solids in liquid.

Our variation analysis showed that in the investigated case

- the dissolution time is not significantly affected by the feeding position in the tank nor by the pumping mode or the viscosity.
- the Re number of the system moderately affects the dissolution time.
- particle size and concentration driving force strongly impact dissolution.
- in contrast to dissolution, mixing is a strong function of the Reynolds number in the system.
- while smaller particles dissolve faster, the mixing time is not reduced significantly.
- scale-up with exact geometric similarity and preserving the Batchelor scale keeps the dissolution time – but not necessarily the mixing time – constant.

In the pharmaceutical development process it is not possible to test every product in all available production devices. Therefore, it is essential to use literature information and prior knowledge as a starting point for the process development. CFD simulations, i.e., the numerical approach, may guide experimentation and may help to understand the impact of various parameters on the process efficiency, especially in the process scale-up. As we could show the change of a single parameter affects mixing and dissolution. Thus, using CFD can significantly reduce development times, and conflicting targets can be managed during the optimization process.

In future studies additional effects will be investigated as well as other tank types, such as baffled-, cylindrical- and cone-shaped tanks, and various impeller types at different locations within the vessel. Furthermore, in order to adjust the dissolution model to various powder types, experimental analysis of the powder properties is required.

AUTHOR INFORMATION

Corresponding Author

*Phone: +43-316-873-7978. Fax: +43-316-873-7963. E-mail: khinast@tugraz.at.

ACKNOWLEDGMENT

This work has been carried out as part of the K1 Competence Center program funded by the Austrian Research Promotion Agency (FFG), State of Styria, and Styrian Business Promotion

Agency (SFG). The authors gratefully acknowledge Mr. Jakob Redlinger-Pohn, Mr. Gregor Toschkoff, and Dr. Heidrun Gruber-Wölfler for their help and useful discussions.

NOTATION

A	[m ²] particle surface
A_p	[m ²] cross-sectional area of the particle
b	[m] impeller blade height
C	[m] bottom clearance
C_μ	[-] model coefficients
c_∞	[mol/m ³] local liquid concentration
C_D	[-] drag coefficient
c_μ, c_{mean}	[mol/m ³] local, averaged concentration
c_s	[mol/m ³] saturation concentration
D	[m] impeller diameter
D_A	[m ² /s] diffusion coefficient
d_p	[m] particle diameter
d_{p0}	[m] initial particle diameter
dt	[s] time step
e	[m] off-center distance
ε	[m ² /s ³] dissipation rate of the turbulent kinetic energy
F_{id}	[N] drag force
F_{ig}	[N] gravity and buoyancy force
F_{ip}	[N] pressure force
Fr	[-] Froude number
g	[m/s ²] gravitational acceleration
Ga	[-] Galilei number
H	[m] filling level
h'	[m] vortex depth
I_u	[-] uniformity index
k	[m ² /s ²] turbulent kinetic energy per unit mass
$k(SL)$	[m/s] mass transfer coefficient (solid–liquid)
L	[m] turbulent length scale
M_G	[kg/mol] molar mass
m_{ip}	[kg] parcel mass
N	[rpm] impeller speed
Ne	[-] Newton number
N_{js}	[rpm] impeller speed just suspend particles
ν_t	[Pa s] eddy viscosity
P	[W] power input
p	[Pa] pressure
r^*	[-] normalized radius
Re	[-] Reynolds number
Re_p	[-] particle Reynolds number
S	[m] submergence of the impeller
Sc	[-] Schmidt number
Sh	[-] Sherwood number
T	[m] vessel diameter
T_m	[m] mean vessel diameter (cone-shaped tank)
T_{max}	[m] largest diameters of the cone part of the vessel
T_{min}	[m] smallest diameters of the cone part of the vessel
t_t	[s] turbulent time scale
t_{turb}	[s] turbulence correlation time
u_i'	[m/s] fluctuation velocity
V_j	[m ³] cell volume of the computational cell j
V_p	[m ³] particle volume
V_{tot}	[m ³] total volume of the domain
z^*	[-] normalized height
X	[%] initial solids mass fraction
η, μ	[Pa s] dynamic viscosity
ν	[m ² /s] kinematic viscosity

ρ [kg/m³] density of the liquid
 ρ_p [kg/m³] density of the particles

REFERENCES

- (1) Zlokarnik, M. *Stirring - Theory and Practice*; Wiley-VCH, 2001; ISBN 3-527-29996-3.
- (2) Paul, E. L.; Atiemo-Obeng, V. A.; Kresta, S. M. *Handbook of industrial mixing: science and practice*; Wiley-IEEE: 2004.
- (3) Shi, J.; Wang, J. D.; Yu, G. C.; Chen, M. H. *Chemical Engineering Handbook*, 2nd ed.; Chemical Industry Press: 1996.
- (4) Versteeg, K. H.; Malalasekera, W. *An introduction to Computational Fluid Dynamics - The Finite Volume Method*; Longman Scientific Technical: 1995.
- (5) Menter, F. R. Two-equation eddy-viscosity turbulence models for engineering applications. *AIChE J.* **1994**, 32 (No. 8), 1598–1605.
- (6) Launder, B. E.; Reece, G. J.; Rodi, W. Progress in the development of a Reynolds-Stress turbulent closure. *J. Fluid Mech.* **1975**, 68 (3), 537–566.
- (7) Bakker, A.; LaRoche, R. D.; Wang, M.; Calabrese, R. V. Sliding mesh simulation of laminar flow in stirred reactors. *The online CFM book* **2000**, 1–8.
- (8) Lamberto, D. J.; Alvarez, M. M.; Muzzio, F. J. Experimental and computational investigation of the laminar flow structure in a stirred tank. *Chem. Eng. Sci.* **1999**, 54 (7), 919–942.
- (9) Wang, Y.; Rao, Q.; Fan, J.; Fei, W. In *PIV measurements and CFD simulation of viscous fluid flow in a stirred tank agitated by a Rushton turbine*, 5th International Conference on CFD in the Process Industries, 2006.
- (10) Aubin, J.; Fletcher, D. F.; Xuereb, C. Modeling turbulent flow in stirred tanks with CFD: the influence of the modeling approach, turbulence model and numerical scheme. *Exp. Therm. Fluid Sci.* **2004**, 28, 431–445.
- (11) Aubin, J.; Mavros, P.; Fletcher, D. F.; Xuereb, J. B. C. Effect of axial agitator configuration (up-pumping, down-pumping, reverse rotation) on flow patterns generated in stirred vessels. *Chem. Eng. Res. Des.* **2001**, 79 (A8), 845–856.
- (12) Montante, G.; Lee, K. C.; Yianneskis, A. B. M. Numerical simulation of the dependency of flow pattern on impeller clearance in stirred vessels. *Chem. Eng. Sci.* **2001**, 56, 3751–3770.
- (13) Kumaresan, T.; Joshi, J. B. Effect of impeller design on the flow pattern and mixing in stirred tanks. *Chem. Eng. J.* **2006**, 115 (Issue 3), 173–193.
- (14) Ciofalo, M.; Brucato, A.; Torracca, F. G. N. Turbulent Flow in closed and free-surface unbaffled tanks stirred by radial impellers. *Chem. Eng. Sci.* **1996**, 51 (14), 3557–3573.
- (15) Ferziger, J. H.; Peric, M. *Computational methods for fluid dynamics*, 3rd rev. ed.; Springer: 2002; ISBN 3-540-42074-6.
- (16) Derksen, J. J. Numerical simulation of solids suspension in a stirred tank. *AIChE J.* **2003**, 49, 2700–2714.
- (17) Derksen, J. Assessment of large eddy simulations for agitated flows. *Trans. IChemE* **2001**, 79, 824–830.
- (18) Hartmann, H.; Derksen, J. J.; van den Akker, H. E. A. Numerical simulation of a dissolution process in a stirred tank reactor. *Chem. Eng. Sci.* **2006**, 61, 3025–3032.
- (19) Hartmann, H.; Derksen, J. J.; Montavon, C.; Pearson, J.; Hamill, I. S.; van den Akker, H. E. A. Assessment of large eddy and RANS stirred tank simulation by means of LDA. *Chem. Eng. Sci.* **2004**, 59, 2419–2432.
- (20) Murthy, B. N.; Joshi, J. B. Assessment of standard k- ϵ , RSM and LES turbulence models in a baffled stirred vessel agitated by various impeller designs. *Chem. Eng. Sci.* **2008**, 63, 5468–5495.
- (21) Hosseini, S.; Patel, D.; Ein-Mozaffari, F.; Mehrvar, M. Study of solid-liquid mixing in agitated tanks through computational fluid dynamics modeling. *Ind. Eng. Chem. Res.* **2010**, 49, 4426–4435.
- (22) Armenante, P. M.; Nagamine, E. U. Effect of low off-bottom impeller clearance on the minimum agitation speed for complete suspension of solids in stirred tanks. *Chem. Eng. Sci.* **1998**, 53, 1751–1775.
- (23) Myers, K. J.; Bakker, A. Solids suspension with up-pumping pitched-blade and high-efficiency impellers. *Can. J. Chem. Eng.* **1998**, 76, 433–440.
- (24) Shekhar, S. M.; Jayanti, S. CFD study of power and mixing time for paddle mixing in unbaffled vessels. *Chem. Eng. Res. Des.* **2002**, 80 (A5), 482–498.
- (25) Guha, D.; Ramachandran, P. A.; Dudukovic, M. P.; Derksen, J. J. Evaluation of large eddy simulation and Euler-Euler CFD models for solids flow dynamics in a stirred tank reactor. *AIChE J.* **2008**, 54, AIChE Journal.
- (26) Özcan-Taskin, G.; Wei, H. The effect of impeller-to-tank diameter ratio on draw down of solids. *Chem. Eng. Sci.* **2003**, 58, 2011–2022.
- (27) Pangarkar, V. G.; Yawalkar, A. A.; Sharma, M. M.; Beenackers, A. A. C. M. Particle-liquid mass transfer coefficient in two-/three-phase stirred tank reactors. *Ind. Eng. Chem. Res.* **2002**, 41, 4141–4167.
- (28) Khazam, O.; Kresta, S. M. A novel geometry for solids draw-down in stirred tanks. *Chem. Eng. Res. Des.* **2009**, 87 (3A), 280–290.
- (29) The United States Pharmacopeia and The National Formulary. In *The Official Compendia of Standards*, USP 29-NF 24 2005, Pharmacopoeial Convention Inc.: Nov., 2005.
- (30) Bai, G. E.; Armenante, P. M.; Plank, R. V. Experimental and computational determination of blend time in USP dissolution testing apparatus II. *J. Pharm. Sci.* **2007**, 96, 3072–3086.
- (31) Bocanegra, L. M.; Morris, G. J.; Jurewicz, J. T.; Mauger, J. W. Fluid and particle laser Doppler velocity measurements and mass transfer predictions for the USP paddle method dissolution apparatus. *Drug Dev. Ind. Pharm.* **1990**, 16, 1441–1464.
- (32) Bai, G. E.; Armenante, P. M.; Plank, R. V.; Gentzler, M.; Ford, K.; Harmon, P. Hydrodynamic investigation of USP dissolution test apparatus II. *J. Pharm. Sci.* **2007**, 96 (No. 9), 2327–2349.
- (33) Kukura, J.; Arratia, P. E.; Szalai, E. S.; Muzzio, F. J. Engineering tools for understanding the hydrodynamics of dissolution tests. *Drug Dev. Ind. Pharm.* **2003**, 29, 231.
- (34) Baxter, J. L.; Kukura, J.; Muzzio, F. J. Hydrodynamics-induced variability in the USP apparatus II dissolution test. *Int. J. Pharm.* **2005**, 292, 17–28.
- (35) Kukura, J.; Baxter, J. L.; Muzzio, F. J. Shear distribution and variability in the USP apparatus 2 under turbulent conditions. *Int. J. Pharm.* **2004**, 279, 9–17.
- (36) McCarthy, L. G.; Bradley, G.; Corrigan, J. C. S. O. L.; Healy, A. M. Computational fluid dynamics modeling of the paddle dissolution apparatus: Agitation rate, mixing patterns, and fluid velocities. *AAPS PharmSciTech* **2004**, 5.
- (37) Bai, G. E.; Armenante, P. M. Hydrodynamic, mass transfer, and dissolution effects induced by tablet location during dissolution testing. *J. Pharm. Sci.* **2009**, 98, 1511–1531.
- (38) Hanjalic, K.; Popovac, M.; Hadziabdic, M. A robust near-wall elliptic-relaxation eddy-viscosity turbulence model for CFD. *Int. J. Heat Fluid Flow* **2004**, 25, 1047–1051.
- (39) Adam, S.; Suzzi, D.; Radeke, C.; Khinast, J. G. An integrated Quality by Design (QbD) approach towards design space definition of a blending unit operation by Discrete Element Method (DEM) simulation. *Eur. J. Pharm. Sci.* **2011**, 42, 106–115.
- (40) Freudig, B.; Hogeekamp, S.; Schubert, H. Dispersion of powders in liquids in a stirred vessel. *Chem. Eng. Process.* **1999**, 38, 525–532.
- (41) Assirellia, M.; Bujalskia, W.; Eagleshamb, A.; Nienow, A. W. Macro- and micromixing studies in an unbaffled vessel agitated by a Rushton turbine. *Chem. Eng. Sci.* **2008**, 63 (1), 35–46.
- (42) Drew, G. R.; Ahmed, N.; Jameson, G. J., An optimum concentration for the suspension of solids in stirred vessels. *Mixing and Crystallization*; Kluwer Academic Publishers: 2000; pp 83–94, ISBN 0-7923-6200-4.
- (43) FIRE Workflow Manager Users Guide. In *AVL User Manual*, FIRE v2009: 2009.
- (44) Patankar, S. V.; Spalding, D. B. A calculation procedure for heat, mass and momentum transfer in three-dimensional parabolic flows. *Int. J. Heat Mass Transfer* **1972**, 15 (10), 1787–1806.

- (45) Durbin, P. A. Near-wall turbulence closure modeling without 'damping functions'. *Theor. Comput. Fluid Dynam.* **1991**, 3, 1–13.
- (46) Couper, J. R.; Penney, W. R.; Walas, J. R. F. S. M. *Chemical process equipment: selection and design*; Butterworth-Heinemann: 2009.
- (47) Dukowicz, J. K. Quasi-Steady Droplet Phase Change in the Presence of Convection. *Informal Report, LA 7997-MS, Los Alamos Scientific Laboratory* 1979.
- (48) Schiller, L.; Naumann, A. Z. A drag coefficient correlation. *VDI Z. (1857-1968)* **1933**, 77, 318–320.
- (49) ICE Physics & Chemistry. In AVL User Manual, FIRE v2009: 2009.
- (50) Graham, D. I.; James, P. W. Turbulent dispersion of particles using eddy interaction models. *Int. J. Multiphase Flow* **1996**, Volume 22, Issue 1, 157–175.
- (51) Nienow, A. W.; Miles, D. Effect of impeller-tank configurations on fluid-particle mass-transfer. *Chem. Eng. J. Biochem. Eng. J.* **1978**, 15, 13–24.
- (52) Chang, C. Y.; Tsai, W. T.; Ing, C. H.; Chang, C. F. Adsorption of polyethylene glycol (PEG) from aqueous solution onto hydrophobic zeolite. *J. Colloid Interface Sci.* **2003**, 260, 273–279.